Multi-layer structure toward simultaneous enhancement of forward osmosis membrane separation performance and anti-biofouling property

Peng-Fei Sun[a,b], Pulak Sarkar[b], Eun-Tae Yun[c], Jeong Hoon Lee[a,d], Chuyang Y. Tang[b], Hee-Deung Park[a,e*]

[a] School of Civil, Environmental and Architectural Engineering, Korea University, Seoul 02841, South Korea

[b] Department of Civil Engineering, The University of Hong Kong, Hong Kong 999077, PR China

[c] Chemical and Environmental Engineering, Yale University, New Haven 06510, United States

[d] Eco Lab Center, SK ecoplant co. Ltd., Seoul 03143, South Korea

[e] KU-KIST Graduate School of Converging Science and Technology, Korea University, Seoul 02841, South Korea

*** Corresponding author**

Postal address: School of Civil, Environmental and Architectural Engineering, Korea University, 145 Anam-Ro, Seongbuk-Gu, Seoul 02841, South Korea

Phone: +82-2-3290-4861

Fax: +82-2-3290-5999

E-mail: heedeung@korea.ac.kr

Graphical abstract

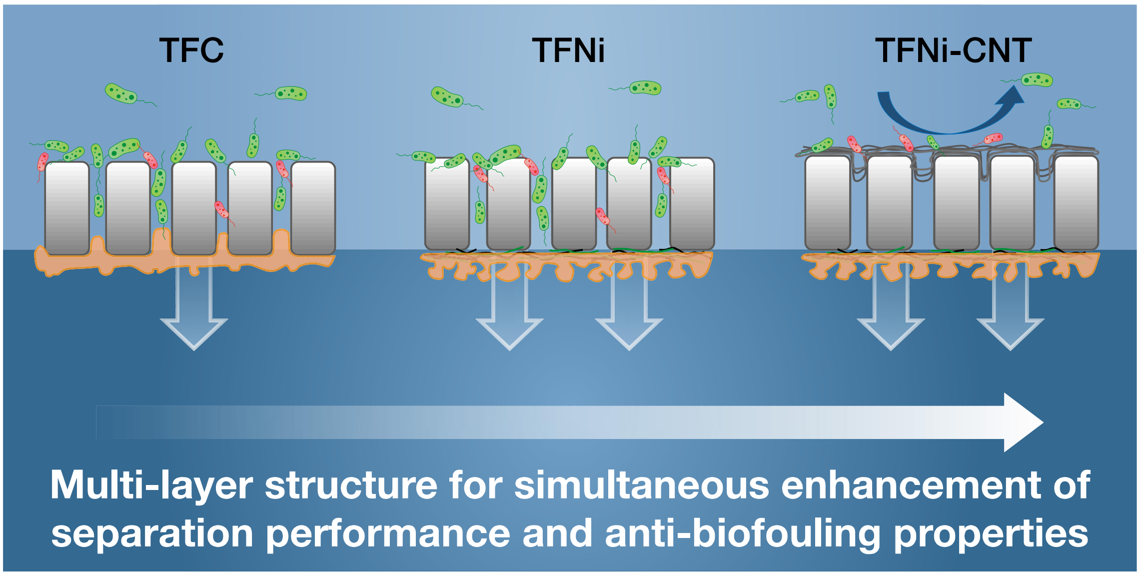

Abstract

Biofouling is a critical issue in membrane-based water-treatment processes because the feed solution retains microorganisms despite rigorous pretreatment. The forward osmosis (FO) process has a drawback of severe biofouling tendency when the active layer faces the draw solution. Here, we fabricated a thin-film nanocomposite membrane with a multilayer structure consisting of an MXene/carbon nanotubes (MXene/CNT) interlayer and a CNT back layer (TFNi-CNT). The interlayer structure significantly enhanced the membrane separation performance whereas the CNT back layer did not significantly hamper the performance. The biofilm formed on the CNT back layer surface was reduced by approximately 90% compared to that on the pristine substrate, indicating that the CNT back layer has superior antibiofilm properties. The water flux of the TFNi-CNT membrane was well-maintained (approximately 46%) and reversibly recovered through facile physical flushing, even after four dynamic biofouling cycles, whereas that of the pristine membrane was reduced to approximately 10%. These results indicated that the TFNi-CNT membrane possesses excellent resistance to biofouling. The CNT layer acts as a barrier that effectively prevents bacteria from entering the inner porous substrate, thus alleviating the detrimental biofilm-enhanced internal concentration polarization. This study provides new insights into the rational design and fabrication of FO membranes to mitigate biofouling.

Keywords: forward osmosis, membrane biofouling, interlayer, MXene, carbon nanotubes

1. Introduction

Population growth and industrialization have accelerated the demand for and dependence on clean water and green energy [1, 2]. Adopting membrane-based technologies can enable advanced wastewater treatment, potable water reuse, and energy recovery [2-4]. The forward osmosis (FO) membrane process, which relies on the osmotic pressure gradient, offers some advantages (e.g., low energy consumption [5, 6] and fouling tendency [7, 8]) compared to conventional pressure-based membrane processes, such as reverse osmosis (RO) and nanofiltration. To date, FO processes have been widely and intensively studied for diverse environmental applications, such as feed solution (FS) (e.g., municipal wastewater [9, 10] and fruit juice [11, 12]) dewatering, draw solution (DS) (e.g., fertilizer [13, 14] and RO brine [15, 16]) dilution, and other hybrid membrane processes (e.g., osmotic membrane bioreactors [17, 18] FO membrane distillation [19, 20]).

Previous studies [8, 21-23] reported that two types of membrane orientations could be adopted for practical FO applications, the active layer-facing feed solution (AL-FS) mode and the active layer-facing draw solution (AL-DS) mode. In the AL-FS mode, the water flux is much lower than that in the AL-DS mode because of more severe internal concentration polarization (ICP) [22, 24]. There are two approaches to reduce the adverse effects of ICP, i.e., the FO membrane orientation can be switched to the AL-DS mode, and the porous support layer (or substrate) encountered with the FS, or, the support layer of the FO membrane can be optimized to decrease the structural parameter (S) value, such as by adapting microfiltration (MF) membranes instead of ultrafiltration membranes because the former is more porous and less torturous [25-27].

However, the above-mentioned AL-DS mode has a risk of causing severe fouling potential. This is because the pore sizes at the backside of the support layer are relatively large, ranging from hundred nanometers to several micrometers [28-30]. As a result, the foulants in the FS are easily carried into the porous support layer, thereby increasing the fouling propensity of the AL-DS mode. Compared to organic or inorganic fouling, biofouling is more intractable because microbes can survive even after rigorous pretreatment [9, 31, 32]. The microorganisms eventually penetrate the internal pores, cause pore clogging, and form a biofilm, thus inducing more severe ICP and irreversibly reducing the water flux [33]. Additionally, the MF substrate is prone to defects because large pores may not be sufficient to support the polyamide layer [26]. Further, the polyamides can also penetrate the substrate, thereby decreasing the water flux. Therefore, the rational design and development of a novel support layer with excellent fouling resistance and support strength are crucial for taking full advantage of the higher water flux of the AL-DS mode.

Many strategies (e.g., polymer coating [34], grafting [35], or in situ growth of nanoparticles [36]) have been proposed to regulate the properties of the support layer to improve fouling resistance (e.g., reduce protein adsorption or bacterial adhesion). Although these approaches can achieve a coating layer along the pore walls, these cannot fully cover the overall surface or shield the large pores of the substrate. FO membranes with a double-skinned layer [29] or an external dense layer [28] on the backside of the substrate have been developed to prevent trapping of foulants in the pores of the substrate. Recently, Deng et al. [37] developed a sandwich-like support layer that exhibited improved separation performance and reduced bovine serum albumin (BSA) adsorption. However, these strategies mainly focus on reducing organic fouling, and their anti-biofouling abilities have rarely been investigated. In particular, using an MF membrane as the support layer, simultaneously utilizing the advantages of fewer ICP effects (i.e., a small *S* value), and realizing long-term anti-biofouling performance, is still a critical challenge.

In this study, we report the fabrication of a thin-film nanocomposite (TFN) membrane, consisting of an MXene/carbon nanotubes (MXene/CNT) interlayer and a CNT back layer (TFNi-CNT membrane), to improve membrane separation performance (e.g., water flux and specific salt flux) as well as biofouling resistance. We expected that the highly porous and interconnected CNT would defend against bacterial adhesion and invasion as well as reduce the negative effects on the membrane itself. The TFNi-CNT membrane was fabricated by depositing a single CNT layer on the bottom of the MF substrate and a CNT-intercalated MXene interlayer on the front of the MF substrate, followed by an interfacial polymerization reaction to form a polyamide rejection layer. The membrane surface morphologies prior to and post interfacial polymerization were systematically characterized. The effect of the CNT barrier layer on membrane separation performance was investigated using a lab-scale FO device. Dynamic fouling experiments were comprehensively performed using a model bacterium to evaluate the long-term antibiofilm and anti-biofouling properties of the TFNi-CNT membrane. The mechanisms underlying their enhanced separation and antifouling performances are discussed. This study provides novel insights into the properties of CNT barrier layers for biofouling mitigation in FO process.

2. Materials and Methods

2.1. Materials and chemicals

Polyethersulfone (PES) MF membrane (pore size: 0.22 μm) was purchased from Yibo Co. Ltd. (Zhejiang, China). Ti_3AlC_2 MAX phase (400 mesh) was provided by Xinxi Technology Co. Ltd. (Foshan, China). Single-walled CNT (diameter: approximately 1.5 nm; length: 1–5 μm) was purchased from NanoLab Inc. (Waltman, MA, USA). Lithium fluoride (LiF) and hydrochloric acid (HCl) were used to synthesize the $Ti_3C_2T_x$ MXene phase. Dopamine hydrochloride, tris (hydroxymethyl) aminomethane (Tris), and sodium dodecylbenzene sulfonate (SDBS) were used to modify the MXene and CNT. *m*-Phenylenediamine (MPD, 99%), 1,3,5-benzenetricarbonyl trichloride (TMC, 98%), and n-hexane ($\geq$ 95%) were purchased from Sigma-Aldrich to perform interfacial polymerization reaction. Deionized (DI) water (Human Power I^+, Korea) was used to prepare the solutions. To compare the membrane performances, two commercially available membranes, namely Toray TFC membranes (Toray Chemical Korea Inc., Seoul, Korea) and HTI TFC membranes (HTI, Albany, OR, USA) were used (details refer to Table S1).

2.2. Modification of the PES MF substrate

Prior to the modification of the PES substrate, the polydopamine (PDA)-modified MXene (PDA/MXene) and polydopamine-modified CNT (PDA/CNT) solutions were firstly prepared. The $Ti_3C_2T_x$ MXene was obtained by exfoliating the MAX using the minimally intensive layer delamination method according to previous studies [38]. Briefly, 1 g Ti_3AlC_2 was slowly added to a mixture of 1.56 g LiF and 20 mL 9M HCl which was then reacted for 24 h at 30 °C. The slurry was then decanted into two 50 mL centrifuge tubes and centrifuged (7–8 times) at 5000 rpm for 5 min. Centrifugation was continued until the precipitate appeared viscous and the upper suspension turned black. The upper suspension was discharged and then the precipitate was redispersed in 50 mL DI water and sonicated with a nitrogen gas flow for 90 min at 4 °C. Finally, the suspension was centrifuged at 3500 rpm for 30 min to obtain the MXene colloidal solution. The synthesized MXene colloidal solution was diluted to approximately 25 μg/L. The detailed modification methodologies for PDA/MXene and PDA/CNT were in accordance with previous studies [9, 39].

The PDA/CNT-modified substrate was prepared by filtering various volumes (corresponding to loadings of 4, 8, 12, and 16 μg/cm^2) of PDA/CNT solution on the backside of the PES MF membrane (Figure 1). The modified substrates were then dried in an oven at 60 °C for 10 min. Similarly, the interlayers (mixture of PDA/MXene and PDA/CNT) were vacuum-filtered on the front side of the CNT-modified substrates. The interlayer loading was predetermined to 24 μg/cm^2 because the membrane separation performance is optimal at this condition [9].

2.3. Fabrication of the TFNi-CNT FO membranes

An active polyamide layer was created on the front surfaces of the different substrates (pristine MF, interlayer-coated MF, and multi-layer-coated MF) via an interfacial polymerization reaction (Figure 1). Briefly, a 2 wt% MPD solution was poured onto the substrate for 3 min, following which the excess solution was removed using a rubber roller. An

0.1 wt% TMC solution (dissolved in hexane) was then immediately introduced onto the MPD-permeant substrate for 1 min to initiate the interfacial polymerization reaction. The active polyamide layer thus created was then rinsed with hexane to remove residual TMC. Finally, the fabricated membranes were placed in an air-drying oven at 60 °C for 10 min to improve the membrane integrity. The pristine membrane (without the interlayer and CNT back layer) was labeled as the thin-film composite (TFC) membrane. The membrane with the MXene/CNT interlayer was denoted as TFNi membrane. Membranes with identical MXene/CNT interlayers and varying loadings of CNT back layers were named TFNi-n membranes, where n indicates the loading (0, 4, 8, 12, or 16 μg/cm^2) of CNT on the backside of the MF substrates.

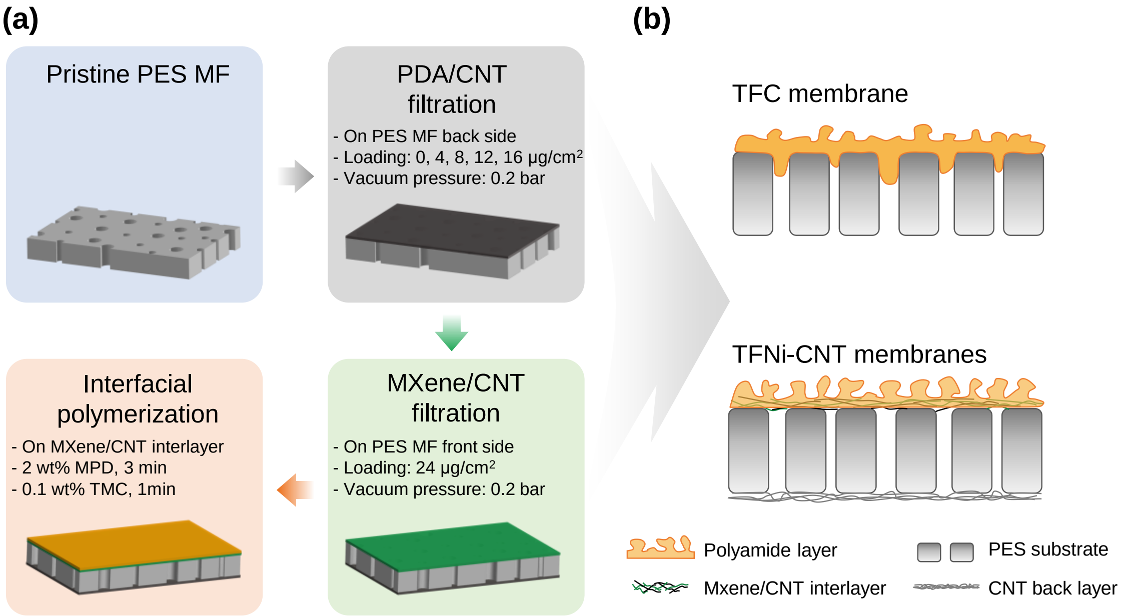

Figure 1. Illustration of the membrane fabrication processes. (a) TFNi-CNT membranes were fabricated by incorporating a CNT back layer and an MXene/CNT interlayer, followed by an interfacial polymerization reaction. (b) Illustration of the structure of obtained TFC and TFNi-CNT membranes.

2.4. Membrane characterization

The surface morphologies of the front and back layers of the fabricated membranes, prior to and post-coating, were observed using field-emission scanning electron microscopy (FE-SEM; Quanta 250 FEG, FEI, USA). The surface roughness of the membranes was evaluated by atomic force microscopy (AFM, NanoWizard II, JPK Instruments) with a scanning area of 5 × 5 µm. Mean roughness (R_a) was determined using the Gwyddion software. The hydrophilicity of the membrane polyamide- and CNT-coated layers were characterized by using a contact angle meter (Attension Theta, Biolin Scientific, Sweden). Membrane surface charge properties were determined using a streaming potential analyzer (SurPASS, Anton Paar, Austria). Membrane surface functional groups of the active polyamide layers were analyzed by using attenuated total reflection Fourier transform infrared spectroscopy (ATR-FTIR; Cary 630, Agilent, USA). X-ray photoelectron spectroscopy (Thermo Scientific K-Alpha, Thermo Fisher Scientific, UK) was used to measure the elemental composition and then calculate the degree of crosslinking based on our previous study [9].

2.5. Evaluation of performances of the FO membrane

The separation performances of the fabricated TFC and TFNi-CNT membranes were measured by using a laboratory-scale FO setup [30]. Specifically, the membrane module, which had an effective filtration area of 9.3 cm^2, was equipped with two diamond spacers in symmetric channels (depth: 2 mm). DI water and 1 M NaCl solution were used as the FS and DS, respectively. A peristaltic pump (Longer Pump, China) was used to circulate the FS and DS at a crossflow velocity of 13 cm/s. Membrane separation performance tests were conducted in AL-FS and AL-DS modes.

The water flux (J_w) was measured according to the changes in DS weight using a balance scale (CUW4200; CAS, Korea). The reverse salt flux (J_s) was measured based on the conductivity variations of the FS and DS using an online probe (Mettler Toledo M300, Switzerland). All the data were continuously logged using a programmable logic controller system. The J_w and J_s can be calculated based on the following equations:

$$J_w = \frac{\Delta m}{A_m \cdot \Delta t \cdot \rho} \qquad (1)$$

$$J_s = \frac{\Delta(C_t \cdot V_t)}{A_m \cdot \Delta t} \qquad (2)$$

where Δm is the mass of permeated water (kg) from FS to DS, A_m is the membrane filtration area (m^2), Δt is the interval time (h), ρ is the density of water (kg/L), and C_t and V_t are the solute concentration (g/L) and FS volume (L), respectively.

2.6. Dynamic antibiofilm assay

Pseudomonas aeruginosa (PA14) was used as a model gram-negative bacterial strain for the antibiofilm and anti-biofouling assays [40, 41]. Briefly, 10 mL of tryptic soy broth (TSB) was inoculated with a single colony of PA14 and incubated with shaking (250 rpm) at 37 ℃ overnight. Thereafter, late exponential stage PA14 cells were centrifuged at 8000 rpm for 5 min at 4 ℃ to discard the TSB medium and then washed twice with sterile synthetic wastewater (the detailed compositions can be found in Table S2 of Supplementary material). The cells were resuspended in 10 mL synthetic wastewater for subsequent tests.

The dynamic antibiofilm performances of the support layers of the TFC and TFNi-CNT membranes were measured using a Drip Flow Biofilm Reactor® (DFR 110, Biosurface

Technologies Corporation, USA) in accordance with previous studies [42, 43]. All equipment for the anti-biofilm assay was sterilized at 121 °C for 15 min. Membrane coupons were prepared and attached to the sterile glass slides. Membrane-attached glass slides were placed in the four DFR channels. Subsequently, 15 mL of 3000 mg/L TSB solution and 1 mL of PA14 were added to each channel. After incubation for 6 h in batch mode at room temperature (approximately 21–23 °C), fresh TSB solution was pumped in a continuous manner into each channel at a flow rate of 50 mL/h using a Masterflex peristaltic pump (Cole-Parmer, Vernon Hills, IL, USA). The reactor was operated for 24 h, and the biofilms formed on the membrane coupons were evaluated using confocal laser scanning microscopy (CLSM, LSM700, Carl Zeiss, Germany) [23, 30].

2.7. Evaluation of anti-biofouling performance

The fabricated TFC and TFNi-12 membranes were selected to estimate the anti-biofouling performance. The biofouling procedures have been detailed in our previous study [30]. Briefly, the PA14 mentioned above was used as the model bacteria. The bacterial concentration was approximately 6.5×10^5 CFU/mL. To eliminate the impact of flux on the bacterial accumulation on the membrane surface or within the pores, the initial flux of TFC and TFNi-12 membranes were purposely kept similar (i.e., 25 LMH) by using different concentrations of NaCl as the DS. The biofouling tests were performed continuously for three days, with one physical flushing every 24 hours. The FS and DS were replaced daily. After the termination of the biofouling tests, the membrane coupons were autopsied for CLSM [23] and FE-SEM analysis.

3. Results and discussion

3.1. Characterization of the CNT-coated substrate

Figure 2 shows the surface morphologies of the backsides of the substrates with and without CNT coating. The pristine PES MF substrate had a relatively large mean pore size (approximately 230 nm, Figure S1) and surface porosity (~ 10.6%) on the backside. With increasing CNT loading on the backside surface, the CNT network gradually covered the pores. The surface pore sizes were dramatically decreased to ~ 10–35 nm as well as the surface porosities were decreased to ~ 2–5% (Figure S1). When the CNT loading was higher than 8 μg/cm^2, the CNT network covered the surface pores completely without affecting their internal structure (Figure S2). The outline of the macropores could be easily discerned from the SEM images, which indicated that the CNT layer was ultrathin. This ultrathin and uniform coating of CNT was expected to create a barrier that prevented microorganisms from penetrating the pores. It is interesting to note that overall pore size exhibited a gradual reduction (i.e., range from ~ 335 nm to ~ 148 nm), while the overall porosity can be well maintained at a certain level (i.e., ~ 73%) (Figure S1). These results indicated that the CNT coating can affect the PES surface characteristics rather than the inside pore structure.

To evaluate the effect of CNT back layer on water transport, the hydraulic resistances of the different layers were further determined based on the resistance-in-series model (Table S3). Although the hydraulic resistance of the CNT back layer was two times higher than the pristine

PES substrate, its absolute value was still much lower (i.e., nearly four orders of magnitude less) than that of the dense polyamide layer. Additionally, the CNTs were modified with hydrophilic PDA, which has been adopted in previous studies to increase the compatibility, adhesion, and stability between CNT and the substrate [25, 44]. Owing to the electrostatic interaction, hydrogen bonding, coordination, and/or covalent reactions [45], the PDA-modified CNT can robustly adhere to the substrate even after continuous physical flushing under relatively high cross-flow velocity (refer to Figures S4, S5 and S6). The CNT-coated PES substrate has a lower water contact angle (approximately 55.1 ± 2.3 °C, Figure 4d). Generally, a more hydrophilic membrane surface has higher surface energy and can facilitate water flow across the membrane [46]. The hydrophilic surface is also beneficial to mitigate the interaction of foulants with membranes, such as humid acid or protein deposition or adhesion on the membrane surface [37, 47]. Therefore, we speculate that the CNT-coated substrate can alleviate the fouling propensity without compromising membrane separation performance.

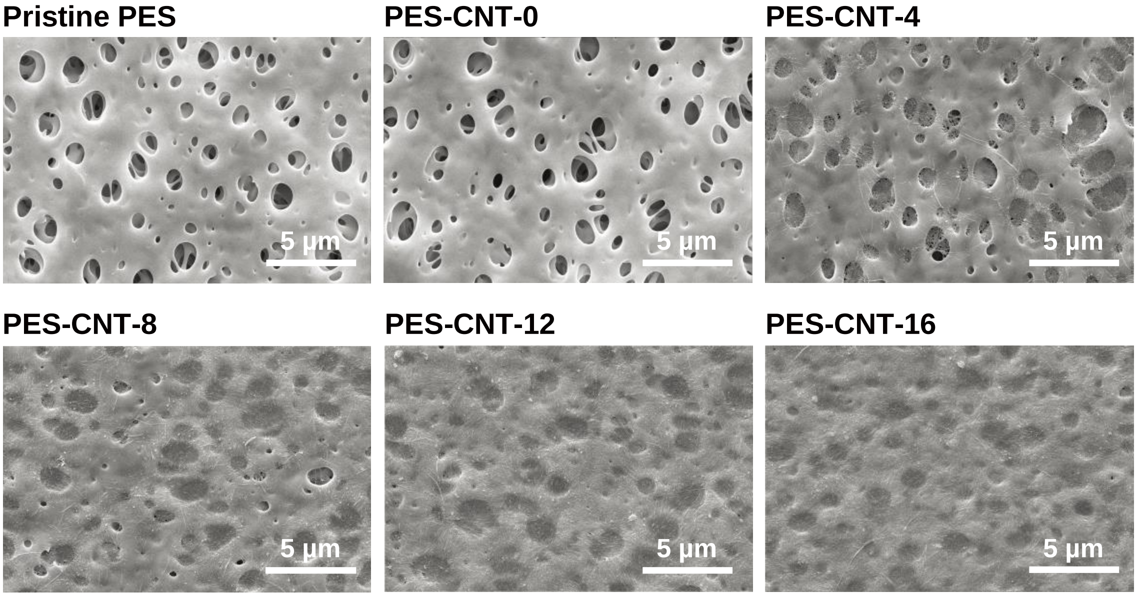

Figure 2. Surface morphologies of the backside of the polyethersulfone (PES) microfiltration substrates coated by carbon nanotubes (CNT) at different loadings. The suffixal numbers 0, 4, 8, 12, and 16 refer to the CNT loading amount (μg/cm^2) on the back side of the PES substrate.

3.2. Characterization of the TFNi-CNT FO membranes

After the CNT were coated onto the backside of the PES MF substrates, a mixture of PDA/MXene and PDA/CNT was similarly deposited on the substrate's upper side as an interlayer (Figure S3). Based on the results of SEM images and FTIR spectra, the deposition of interlayer exhibited insignificant influences on the microscopic structure (e.g., the surface porosity and morphology) of the CNT back layer. We speculated that the PDA modification of CNT and the experimental conditions (e.g., post-treatment of heating, low vacuum pressure, etc.) for preparing the CNT back layer and interlayer may mutually enhance the stability of the CNT back layer.

A polyamide rejection layer was then fabricated via interfacial polymerization (Figure 1). The ATR-FTIR spectra (Figure 4a) revealed that the polyamide was successfully formed on the surface of the pristine as well as interlayered PES MF substrates. Notably, the polyamide of the TFC membrane appeared relatively flat, with fewer small nodules, even those formed in the internal pores (Figure 3a). In contrast, the TFNi-CNT membranes exhibited typical characteristics of the polyamide rejection layer featuring more abundant “ridge-and-valley” morphologies, which could also be evidenced by their larger surface roughness (Figure 3b and Table S4). This significant difference can be attributed to the incorporation of an interlayer. Previous studies [48] have revealed that the interlayer can play versatile roles in facilitating polyamide layer formation. On the one hand, the interlayer can improve monomer adsorption and thus be beneficial in forming a better-quality active polyamide layer. On the other hand, it can provide a new interface, which not only prevents the polyamide from invading the large pores of substrate (approximately 200 nm in this study) but also enhances nanobubble generation during the interfacial polymerization reactions. These factors could have contributed to the polyamide layers of all interlayered TFNi-CNT membranes showing a dual-layer structure (i.e., a top exterior layer and a basal nodular layer [49]) in this study, with a larger leaf size and a rougher surface (Figure 3b).

In addition, the interlayer structure can alter the physicochemical properties of the subsequent polyamide layer. For instance, the surface zeta potential (Figure 4b) exhibited significant differences between the TFC and the interlayered membranes (i.e., TFNi-CNT membranes). The zeta potential of the TFC membrane gradually decreased from 12.6 mV to -51.9 mV with the increase of pH values from approximately 3 to 10. It is interesting to note that the TFNi-CNT membranes possess very narrow changes in the surface zeta potentials (e.g., nearly within the range from +4 mV to -5 mV), which were consistent with previous studies [26, 39, 50]. Generally, the surface charge is associated with the residual carboxylic acid groups of the polyamide after interfacial polymerization. Highly cross-linked polyamide exhibited a lower number of carboxylic acid groups. Therefore, compared to the TFC membrane, the polyamide layer of TFNi-CNT membranes with high cross-linking degrees (Figure 4c) was less negatively charged due to the decreased deprotonation of carboxylic acid groups.

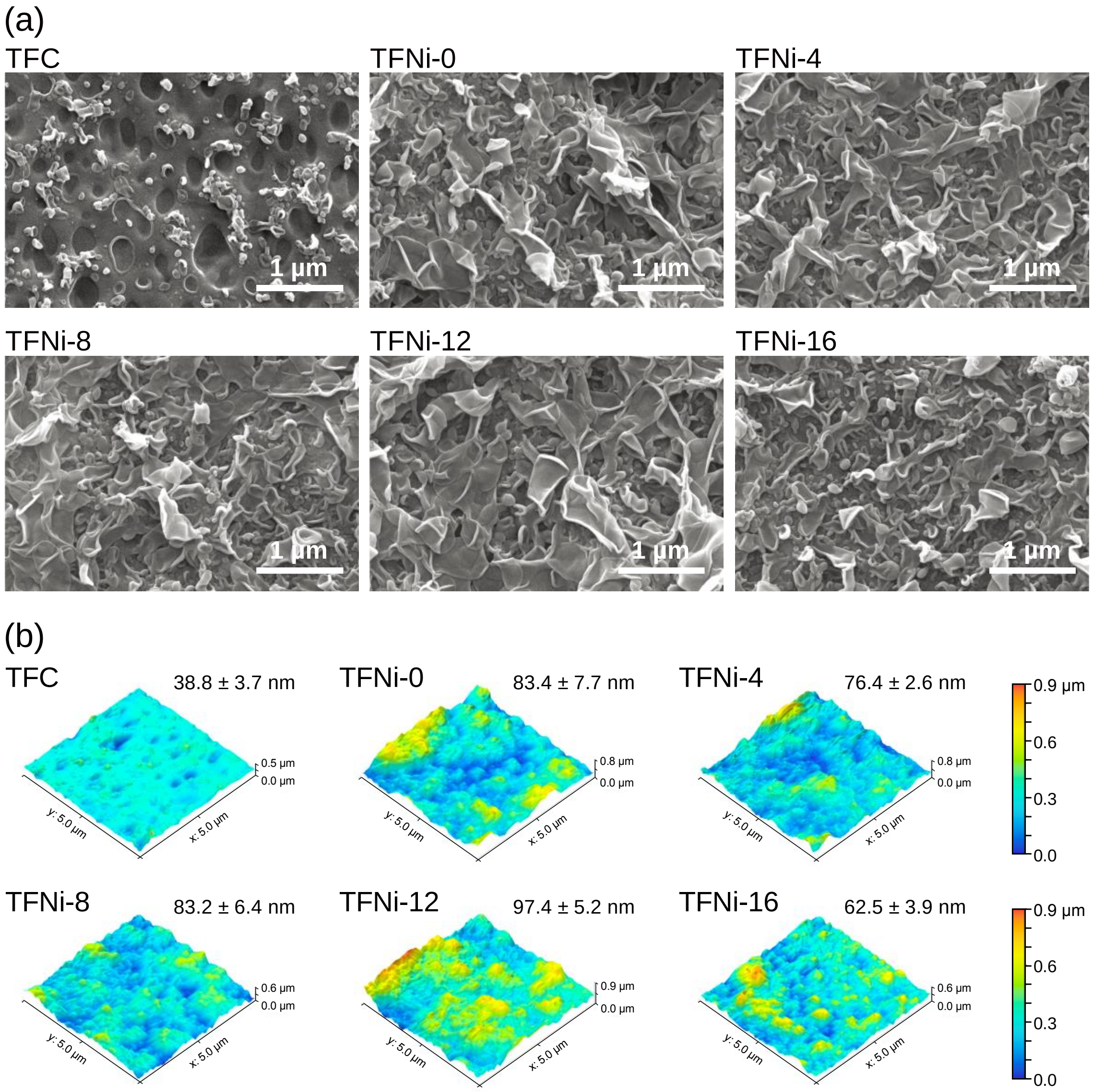

Figure 3. Surface characteristics of the polyamide layer of the TFC and TFNi-CNT membranes. (a) and (b) are the SEM and AFM images with different CNTs loadings on the back layer, respectively. The suffixal numbers 0, 4, 8, 12, and 16 refer to the CNT loading amount (μg/cm^2) on the back side of the PES substrate. The arithmetic average roughness (R_a) values inserted in the AFM images were calculated from at least three replicate measurements.

Additionally, the morphologies of the upper polyamide layer showed no noticeable changes, even with an increase in the coating amount of the CNT back layer. As mentioned above, the interlayer was identical for all TFNi-CNT membranes. Thus, we can speculate that the CNT coating on the backside of the PES MF substrate has no significant influence on polyamide layer formation. Other physicochemical properties, such as membrane surface zeta potential, cross-linking degree, and hydrophilicity, were also systematically determined (Figure 4). Further proving that the CNT barrier layer with an appropriate loading (0–12 μg/cm^2), has no direct impact on the polyamide formation. These results could be predicted because the interfacial polymerization reaction mainly occurred at the surface of the PES substrate or the modified PES substrate (coated with the PDA/MXene/CNT interlayer), and the backside properties of the PES substrate would have very little impact on the polyamide layer.

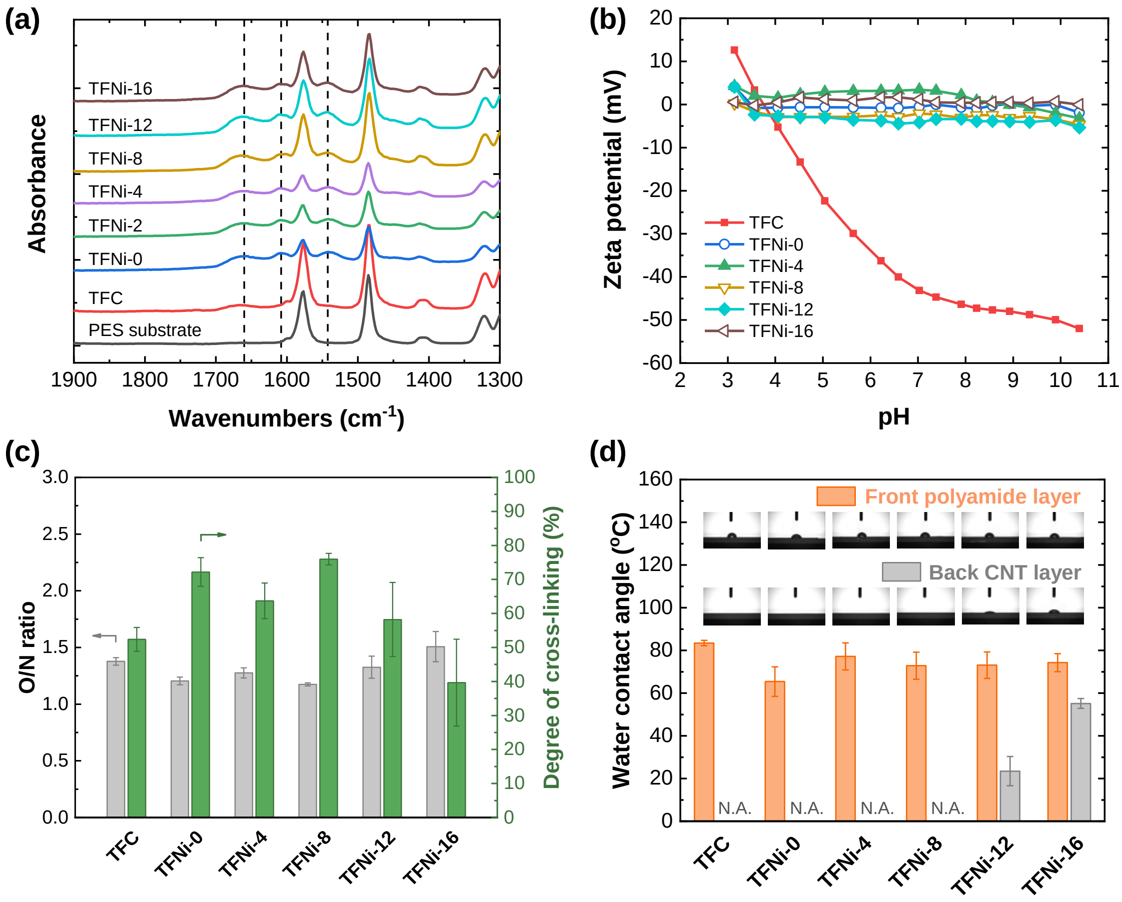

Figure 4. Physicochemical properties of the polyamide layer and CNT-coated back layer of the TFC and TFNi-CNT membranes. (a) ATR-FTIR spectra of the PES MF substrate and the polyamide surface. (b) Zeta potential of the polyamide surface. (c) The oxygen and nitrogen (O/N) ratio as well as the degree of cross-linking of the polyamide surface. (d) The water contact angle of the polyamide layer and CNT-coated back layer. The N.A. symbol means the contact angle cannot be measured (complete wetting) when the water droplet contacts the membrane for 10 seconds. The suffixal numbers 0, 4, 8, 12, and 16 refer to the CNT loading amount (μg/cm^2) on the back side of the PES substrate. Error bars indicate that the tests were performed at least in triplicate.

3.3. Separation performance of the TFNi-CNT FO membranes

The resulting TFC and TFNi-CNT FO membranes were comprehensively evaluated in AL-DS and AL-FS modes (Figure 5). Overall, the TFNi-CNT membranes with an interlayer achieved a much higher water flux (43.5–56.6 LMH and 22.5–25.8 LMH in the AL-DS and AL-FS mode, respectively) compared to the TFC membrane (13.1 LMH and 9.2 LMH in the AL-DS and AL-FS mode, respectively). Moreover, compared with commercially available FO membranes, the TFNi membranes exhibited superior or comparable performances in both modes. Moreover, the specific salt fluxes of the TFNi-CNT membranes were lower than those of the pristine TFC and HTI FO membranes. These unprecedented enhancements in separation performance can be attributed to the active roles played by the interlayer. First, the interlayer-induced richer structure (exterior layer [49]) and rougher surface morphologies (leaf-like) of the polyamide layer can provide more effective filtration areas for faster water transport. Second, the interlayer can alter the water transport pathway through the polyamide layer with minimum hydraulic resistance and then gather these to flow into the substrate, known as the “gutter effect” [48].

Notably, the additional CNT back layer did not significantly affect the water flux due to its hydraulic resistance only–accounting for a very small proportion of the total membrane hydraulic resistance (Table S3). A previous model simulation demonstrated that a low rejection layer as the external feed skin could minimize the overall hydraulic resistance and reduce adverse ICP effects [51]. Generally, a loose back layer formed on the reverse side of the dense top layer can provide additional selectivity for the solute and thus decrease the apparent salt permeability, as demonstrated by previous experimental and modeling results [51, 52].

However, in this study, the trend of specific salt flux gradually increased from 0.30 g/L and 0.35 g/L for the TFNi-0 membrane to 0.66 g/L and 0.63 g/L for the TFNi-16 membrane in two different modes (Figure 5). The fabrication sequencing of the loose back layer and dense top layer primarily governed these opposite results. For instance, the dense layer (polyamide) was first formed on the top of the substrate, followed by a loose layer at the bottom of the substrate. The loose back layer was deposited by surface coating, spraying, or other approaches which did not affect the properties of the top layer. In contrast, the back layer that was first deposited (i.e., the CNT back layer in this study) could have altered the substrate properties to some extent, further changing the characteristics of the polyamide layer (e.g., roughness and degree of cross-linking at higher CNT loadings, see Figure 3c, Table S4, and Figure 4c).

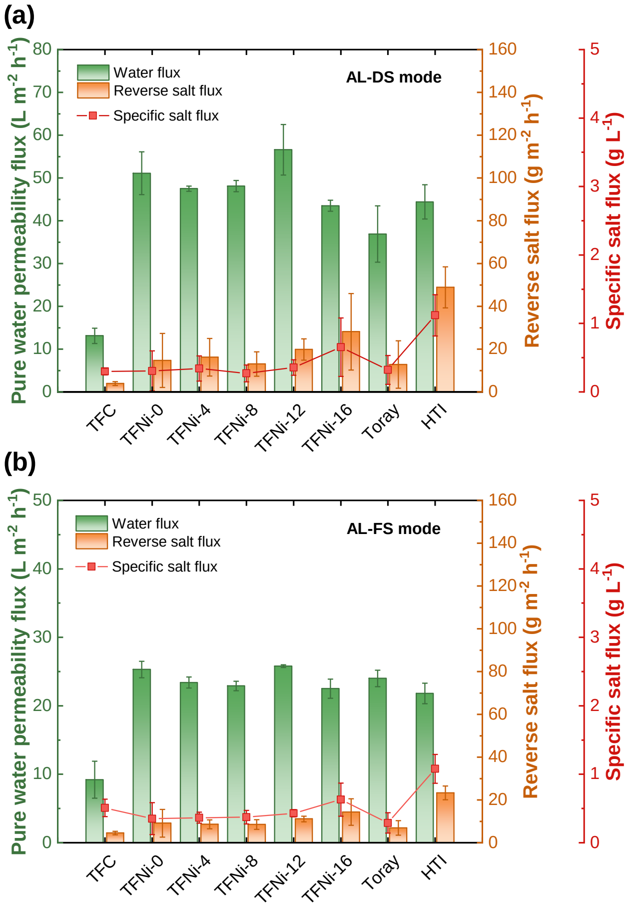

Figure 5. Comparison of the separation performances (water flux, reverse salt flux, and specific salt

flux) of the control TFC and TFNi membranes with other commercially available FO membranes. (a) Active layer-facing draw solution (AL-DS) mode and (b) active layer-facing feed solution (AL-FS) mode. The suffixal numbers 0, 4, 8, 12, and 16 refer to the CNT loading amount (μg/cm^2) on the back side of the PES substrate. DI water and a 1 M NaCl solution were used as the feed solution and draw solution, respectively. Error bars indicate that the tests were performed at least in triplicate.

3.4. Antibiofilm performance of the TFNi-CNT membrane support layer

Prior to evaluating the biofouling resistance of the TFNi-CNT membranes, dynamic biofilm formation tests were carried out to investigate the antibiofilm capacity of the CNT coating. Generally, biofilm developed on the surface of the back layer decreased with the increase in CNT loading (Figure 6a). The biofilm was almost invisible when the loading exceeded 8 μg/cm^2. Furthermore, the characteristics of the biofilm structure on the back layer surface, such as the biovolume and thickness were found to be dramatically reduced by approximately 80–90% in the TFNi-CNT membranes (Figures 6b and 6c) as compared to the control TFC membrane. These results demonstrated that the CNT-coated back layer possessed excellent resistance to biofilm formation.

Notably, the ratio of dead to live cells decreased continuously from 0.98 to 0.30 with the increase in CNT loading from 0 to 16 μg/cm^2, which suggests that the surface of the CNT-coated layer may not be involved in the direct inactivation of the microorganisms during the formation of the biofilm. In this study, PDA, one of the most versatile coating materials with many desirable properties (e.g., hydrophilicity and strong adhesion), was used to modify the CNT. Although many studies have revealed that nanomaterials (e.g., AgNPs, CNT, and GO) can effectively inactivate microorganisms via contact killing and thus reduce biofilm development [36, 53-55], the planktonic bacteria in the FS would directly interact with PDA rather than the CNT. Therefore, we speculated that the anti-biofilm properties may not be rendered by the CNT itself. Compared to the back layer of pristine PES, the CNT-coated back layer exhibited much smaller surface pore size (i.e., ~ 10–35 nm) and porosity (i.e., ~ 2–5%) (Figure S1), which may play a critical role in the reduction of biofilm formation due to the bacteria cannot penetrate the smaller pores and thus reducing the probability of adhesion.

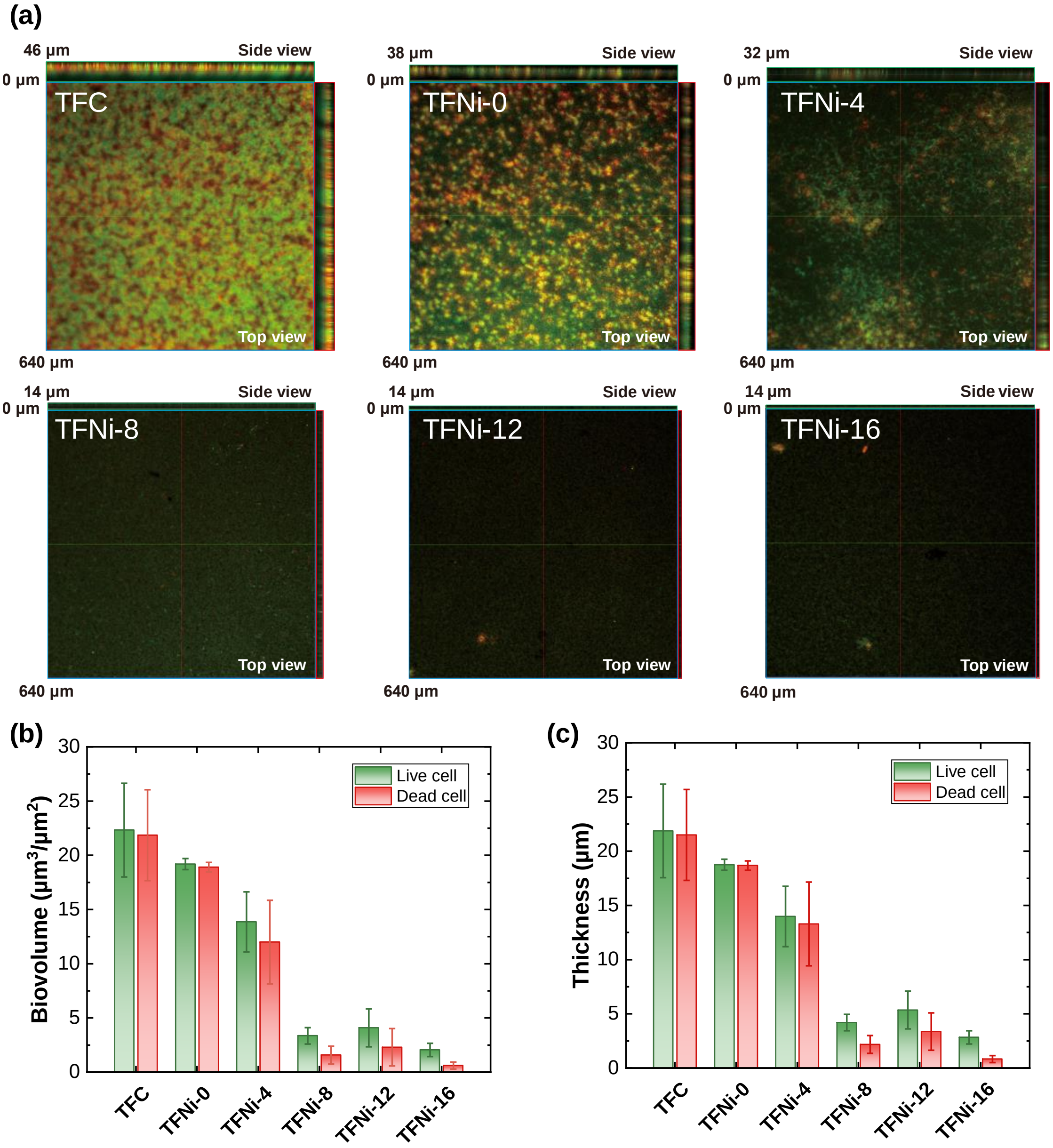

Figure 6. Characteristics of the biofilm formed on the back surface of the TFC and TFNi-CNT membranes. (a) CLSM images of the biofilm developed after a 24 h run of the drip-flow reactor. (b) Average biovolume and (c) thickness of the biofilm formed on the backside surface of different membranes. The suffixal numbers 0, 4, 8, 12, and 16 refer to the CNT loading amount (μg/cm^2) on the back side of the PES

substrate. Error bars represented the standard deviation of data based on at least three different CLSM images.

3.5. Anti-biofouling performance of the TFNi-CNT membranes

Based on the results of the antibiofilm test, TFC and TFNi-12 membranes were selected to investigate their resistance to dynamic biofouling. Figure 7a shows the water flux reduction trends for the TFC and TFNi-12 membranes during the four fouling cycles. The water fluxes of the TFC and TFNi-12 membranes decreased during the first 20 h. After the first biofouling event, the flux decreased to approximately 40% and 51% of the initial flux for the TFC and TFNi-12 membranes, respectively. However, the water flux discrepancy between the TFC and TFNi-12 membranes gradually increased with the number of biofouling cycles. The water flux of the TFC membrane exhibited a dramatic decline (an almost 90% reduction) during the third cycle of biofouling.

After 24 h of biofouling, the membranes were physically cleaned by elevating the crossflow velocity for 30 min. Periodic physical cleaning is one of the most common and facile approaches for alleviating membrane fouling [56]. The flux recovery ratio was calculated to assess cleaning efficiency and fouling reversibility, as shown in Figure 7b. The water flux of the TFC membrane recovered to 76%, 62%, and 19% of the initial flux after the first, second, and third cycles of physical flushing, respectively. In contrast, the TFNi-12 membrane exhibited superior biofouling resistance, as evidenced by the highly recovered flux (approximately 76%, 69%, and 66% of the initial flux after the first, second, and third cleaning cycles, respectively). Our results revealed that biofouling of the TFNi-12 membrane was reversible, whereas the TFC membrane suffered from severe irreversible biofouling. Moreover, a membrane autopsy was performed to further analyze the biofilm that eventually formed on the membrane surface. The SEM and CLSM images (Figure 8) show that abundant biomass accumulated on the TFC membrane surface, whereas only scattered bacterial aggregation and sparse biofilms (amounting to approximately 28% reduction) appeared on the TFNi-12 membrane surface. These results illustrate that the TFNi-CNT membrane can effectively mitigate biofouling.

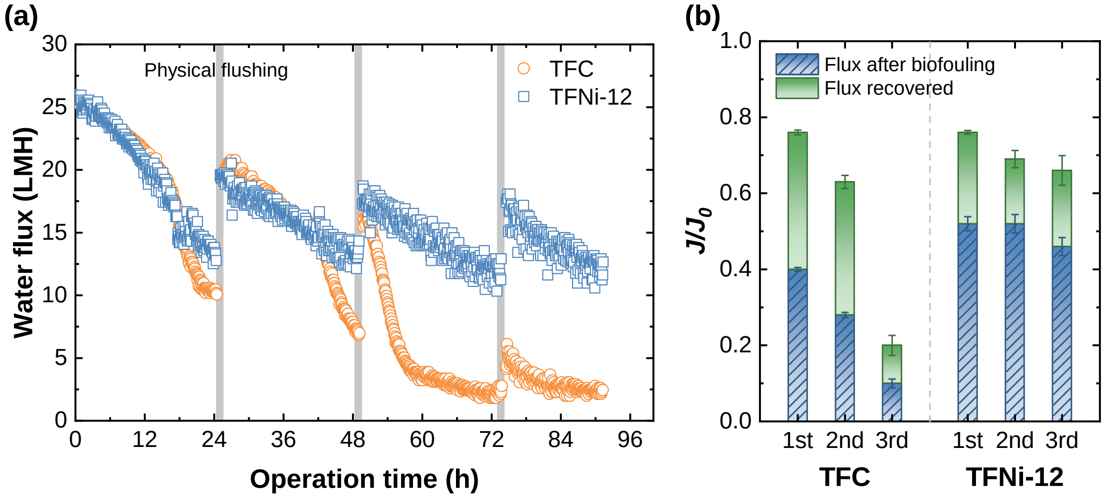

Figure 7. The anti-biofouling performances of the TFC and TFNi-CNT membranes. (a) Water flux decline trends of the TFC and TFNi-12 membranes as a function of operational time. (b) Flux recovery of the two membranes after each physical flushing. Other experimental conditions included physical flushing by doubling the crossflow velocity (to approximately 33.3 cm/s) thrice during the operation. The initial water flux of the two membranes was adjusted to approximately 25 LMH by regulating the concentration of the draw solution.

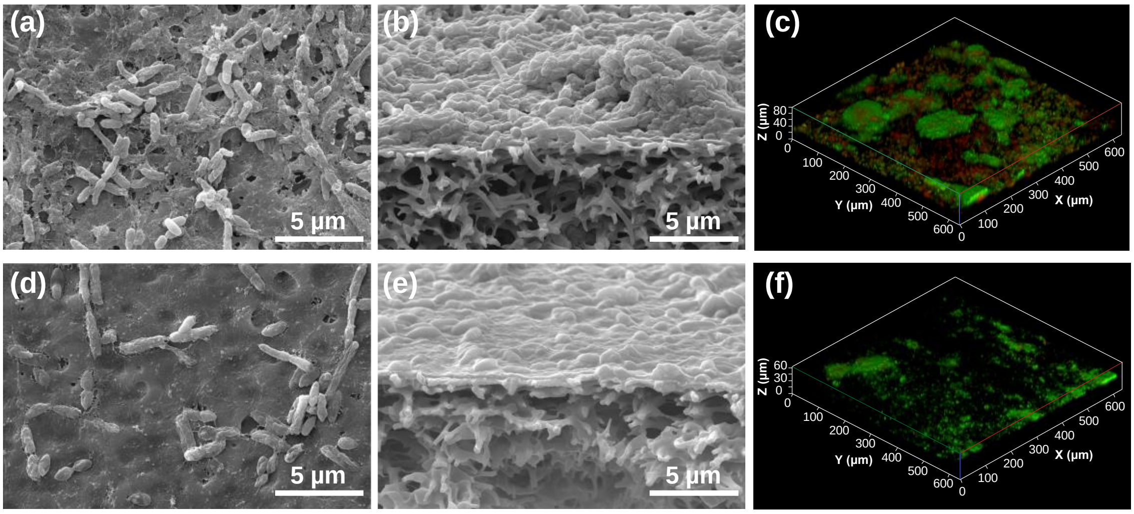

Figure 8. Surface morphologies of the bio-fouled back layer of the TFC and TFNi-CNT membranes after four cycles of biofouling. (a) and (b) is the plan and cross-sectional view of the fouled TFC membrane, and (c) is the corresponding CLSM image. (d) and (e) is the plan and cross-sectional view of the fouled TFNi-12 membrane, and (c) is the corresponding CLSM image.

3.6. Implications

As mentioned in Section 3.4, the TFC membrane without a CNT-coated back layer was more prone to bacterial adherence and biofilm formation on the surface. For the back layer of TFC membrane, it exhibited a relatively larger surface pore size (i.e., ~ 230 nm) and porosity (i.e., ~ 10.6%) based on the SEM image analysis (Figure S1). Indeed, under the dynamic filtration conditions in the AL-DS mode, in addition to adhering to the surface, the bacteria ineluctably penetrate into the relatively large pores owing to the dragging force caused by the water flow [28, 30, 33]. It is almost impossible to remove the biofilm once it forms in the internal structure, even after backwashing [33]. In this case, both the detrimental effects of the biofilm-enhanced ICP and the resistance caused by the biofilm itself led to a sharp decrease in the water flux (Figure 7a). In contrast, CNT coating with denser structure (i.e., reduced surface pore size and porosity, Figure S1) acted as a physical barrier, which not only mitigated bacterial deposition or adhesion but also effectively prevented bacteria from entering the substrate pores. Thus, the biofilm could develop only on the external surface and was easily detached by increasing the hydraulic shear force, such as flushing. Thus, the TFNi-12 membrane possessed superior anti-biofouling properties (Figures 7a and 8).

Further observational approaches need to be applied to obtain more refined and quantitative explanations. For instance, compared to the dense polyamide layer, the additional CNT back layer may not significantly increase the hydraulic resistance, owing to the relatively low CNT loading (2–16 μg/cm^2), which can be quantitatively analyzed using the resistance-in-series model to obtain an intuitive understanding [52, 57]. More advanced analyses, such as quartz crystal microbalance [58-60], and XDLVO theory [61, 62] could be used to further evaluate the interface interaction between the CNT-coated back layer and microorganisms.

A previous study [37] reported similar results in which the back layer could effectively reduce organic fouling (using BSA as a model foulant) owing to the improved hydrophilicity as well as preventing foulants from entering the substrate. Indeed, some matter with lower molecular weights may still pierce the defense barrier (e.g., the CNT-coating layer) and then accumulate within the substrate. For biofouling, essential biofilm constituent substances, such as extracellular polymeric substances, can significantly alter biofilm properties and further influence the fate of biofouling. Once a biofilm forms on the membrane surface, it may also act as a natural biological barrier to sieve or degrade other matter (e.g., ammonia [63] and emerging contaminants [64]) more effectively.

4. Conclusions

In this paper, we report the fabrication of a thin-film nanocomposite membrane with a multilayer structure consisting of a MXene/CNT interlayer and a CNT back layer (TFNi-CNT). The TFNi-CNT membrane with an interlayer structure exhibited excellent FO separation performance (approximately 2.4–3.9 folds higher water flux) compared to the TFC membrane. Notably, because of the relatively low loading amount, the CNT back layer did not significantly affect the membrane separation performance. The results of the dynamic biofilm formation assay confirmed that no obvious biofilms developed on the CNT-coated back surface of the substrate because the CNT back layer mitigated bacterial adhesion. Benefiting from the CNT barrier layer, the TFNi-CNT membranes possess excellent biofouling resistance to maintain water flux. A large portion of the water flux was recovered via facile physical flushing, even after several cycles of biofouling. This study provides a new perspective into the rational membrane design and development to mitigate biofouling.

Declaration of competing interest

The authors declare that they have no competing financial interests or personal relationships that may have influenced the work reported in this study.

Funding

This study was supported by the Basic Science Research Program through the National Research Foundation of Korea (NRF) funded by the Ministry of Education (2020R1A6A1A03045059).

Acknowledgments

References

[1] M.A. Shannon, P.W. Bohn, M. Elimelech, J.G. Georgiadis, B.J. Mariñas, A.M. Mayes, Science and technology for water purification in the coming decades, Nature 452(7185) (2008) 301-310. https://doi.org/10.1038/nature06599.

[2] B.E. Logan, M. Elimelech, Membrane-based processes for sustainable power generation using water, Nature 488(7411) (2012) 313-9. https://doi.org/10.1038/nature11477.

[3] M. Elimelech, W.A. Phillip, The future of seawater desalination: energy, technology, and the environment, Science 333(6043) (2011) 712-7. https://doi.org/10.1126/science.1200488.

[4] C.Y. Tang, Z. Yang, H. Guo, J.J. Wen, L.D. Nghiem, E. Cornelissen, Potable Water Reuse through Advanced Membrane Technology, Environ. Sci. Technol. 52(18) (2018) 10215-10223. https://doi.org/10.1021/acs.est.8b00562.

[5] R. Lambrechts, M.S. Sheldon, Performance and energy consumption evaluation of a fertiliser drawn forward osmosis (FDFO) system for water recovery from brackish water, Desalination 456 (2019) 64-73. https://doi.org/10.1016/j.desal.2019.01.016.

[6] R. Valladares Linares, Z. Li, V. Yangali-Quintanilla, N. Ghaffour, G. Amy, T. Leiknes, J.S. Vrouwenvelder, Life cycle cost of a hybrid forward osmosis – low pressure reverse osmosis system for seawater desalination and wastewater recovery, Water Res. 88 (2016) 225-234. https://doi.org/10.1016/j.watres.2015.10.017.

[7] B. Mi, M. Elimelech, Organic fouling of forward osmosis membranes: Fouling reversibility and cleaning without chemical reagents, J. Membr. Sci. 348(1) (2010) 337-345. https://doi.org/10.1016/j.memsci.2009.11.021.

[8] Q. She, R. Wang, A.G. Fane, C.Y. Tang, Membrane fouling in osmotically driven membrane processes: A review, J. Membr. Sci. 499 (2016) 201-233. https://doi.org/10.1016/j.memsci.2015.10.040.

[9] P.-F. Sun, Z. Yang, X. Song, J.H. Lee, C.Y. Tang, H.-D. Park, Interlayered Forward Osmosis Membranes with Ti3C2Tx MXene and Carbon Nanotubes for Enhanced Municipal Wastewater Concentration, Environ. Sci. Technol. 55(19) (2021) 13219-13230. https://doi.org/10.1021/acs.est.1c01968.

[10] X. Bao, Q. Wu, W. Shi, W. Wang, H. Yu, Z. Zhu, X. Zhang, Z. Zhang, R. Zhang, F. Cui, Polyamidoamine dendrimer grafted forward osmosis membrane with superior ammonia selectivity and robust antifouling capacity for domestic wastewater concentration, Water Res. 153 (2019) 1-10. https://doi.org/10.1016/j.watres.2018.12.067.

[11] K. Zhang, X. An, Y. Bai, C. Shen, Y. Jiang, Y. Hu, Exploration of food preservatives as draw solutes in the forward osmosis process for juice concentration, J. Membr. Sci. 635 (2021) 119495. https://doi.org/10.1016/j.memsci.2021.119495.

[12] X. An, Y. Hu, N. Wang, Z. Zhou, Z. Liu, Continuous juice concentration by integrating forward osmosis with membrane distillation using potassium sorbate preservative as a draw solute, J. Membr. Sci. 573 (2019) 192-199. https://doi.org/10.1016/j.memsci.2018.12.010.

[13] S. Li, Y. Kim, L. Chekli, S. Phuntsho, H.K. Shon, T. Leiknes, N. Ghaffour, Impact of reverse nutrient diffusion on membrane biofouling in fertilizer-drawn forward osmosis, J. Membr. Sci. 539 (2017) 108-115. https://doi.org/10.1016/j.memsci.2017.05.074.

[14] S. Phuntsho, H.K. Shon, T. Majeed, I. El Saliby, S. Vigneswaran, J. Kandasamy, S. Hong, S. Lee, Blended Fertilizers as Draw Solutions for Fertilizer-Drawn Forward Osmosis Desalination, Environ. Sci. Technol. 46(8) (2012) 4567-4575. https://doi.org/10.1021/es300002w.

[15] Y. Kim, Y.C. Woo, S. Phuntsho, L.D. Nghiem, H.K. Shon, S. Hong, Evaluation of fertilizer-drawn forward osmosis for coal seam gas reverse osmosis brine treatment and sustainable agricultural reuse, J. Membr. Sci. 537 (2017) 22-31. https://doi.org/10.1016/j.memsci.2017.05.032.

[16] Y. Xu, Y.-N. Wang, J.Y. Chong, R. Wang, Thermo-responsive nonionic amphiphilic copolymers as draw solutes in forward osmosis process for high-salinity water reclamation, Water Res. 221 (2022) 118768. https://doi.org/10.1016/j.watres.2022.118768.

[17] X. Zhu, L.W. Lee, G. Song, X. Zhang, Y. Gao, G. Yang, S. Luo, X. Huang, Deciphering mono/multivalent draw solute-induced microbial ecology and membrane fouling in anaerobic osmotic membrane bioreactor, Water Res. 209 (2022) 117869. https://doi.org/10.1016/j.watres.2021.117869.

[18] G. Yuan, Y. Tian, B. Wang, X. You, Y. Liao, Mitigation of membrane biofouling via immobilizing Ag-MOFs on composite membrane surface for extractive membrane bioreactor, Water Res. 209 (2022) 117940. https://doi.org/10.1016/j.watres.2021.117940.

[19] M. Li, K. Li, L. Wang, X. Zhang, Feasibility of concentrating textile wastewater using a hybrid forward osmosis-membrane distillation (FO-MD) process: Performance and economic evaluation, Water Res. 172 (2020) 115488. https://doi.org/10.1016/j.watres.2020.115488.

[20] Y. Kim, S. Li, L. Francis, Z. Li, R.V. Linares, A.S. Alsaadi, M. Abu-Ghdaib, H.S. Son, G. Amy, N. Ghaffour, Osmotically and Thermally Isolated Forward Osmosis–Membrane Distillation (FO–MD) Integrated Module, Environ. Sci. Technol. 53(7) (2019) 3488-3498. https://doi.org/10.1021/acs.est.8b05587.

[21] Q. She, X. Jin, Q. Li, C.Y. Tang, Relating reverse and forward solute diffusion to membrane fouling in osmotically driven membrane processes, Water Res. 46(7) (2012) 2478-86. https://doi.org/10.1016/j.watres.2012.02.024.

[22] C.Y. Tang, Q. She, W.C.L. Lay, R. Wang, A.G. Fane, Coupled effects of internal concentration polarization and fouling on flux behavior of forward osmosis membranes during humic acid filtration, J. Membr. Sci. 354(1-2) (2010) 123-133. https://doi.org/10.1016/j.memsci.2010.02.059.

[23] P.-F. Sun, Y. Jang, S.-Y. Ham, H. Ryoo, H.-D. Park, Effects of reverse solute diffusion on membrane biofouling in pressure-retarded osmosis processes, Desalination 512 (2021) 115145. https://doi.org/10.1016/j.desal.2021.115145.

[24] G.T. Gray, J.R. McCutcheon, M. Elimelech, Internal concentration polarization in forward osmosis: role of membrane orientation, Desalination 197(1) (2006) 1-8. https://doi.org/10.1016/j.desal.2006.02.003.

[25] Z. Zhou, Y. Hu, C. Boo, Z. Liu, J. Li, L. Deng, X. An, High-Performance Thin-Film Composite Membrane with an Ultrathin Spray-Coated Carbon Nanotube Interlayer, Environ. Sci. Technol. Lett. 5(5) (2018) 243-248. https://doi.org/10.1021/acs.estlett.8b00169.

[26] G. Gong, P. Wang, Z. Zhou, Y. Hu, New insights into the role of an interlayer for the fabrication of highly selective and permeable thin-film composite nanofiltration membrane, ACS Appl. Mater. Interfaces (2019). https://doi.org/10.1021/acsami.8b18719.

[27] L. Huang, J.R. McCutcheon, Impact of support layer pore size on performance of thin film composite membranes for forward osmosis, J. Membr. Sci. 483 (2015) 25-33. https://doi.org/10.1016/j.memsci.2015.01.025.

[28] M. Hu, S. Zheng, B. Mi, Organic Fouling of Graphene Oxide Membranes and Its Implications for Membrane Fouling Control in Engineered Osmosis, Environ. Sci. Technol. 50(2) (2016) 685-693. https://doi.org/10.1021/acs.est.5b03916.

[29] P.H.H. Duong, T.-S. Chung, S. Wei, L. Irish, Highly Permeable Double-Skinned Forward Osmosis Membranes for Anti-Fouling in the Emulsified Oil–Water Separation Process, Environ. Sci. Technol. 48(8) (2014) 4537-4545. https://doi.org/10.1021/es405644u.

[30] P.-F. Sun, T.-S. Kim, H.-S. Kim, S.-Y. Ham, Y. Jang, Y.-G. Park, C.Y. Tang, H.-D. Park, Improved anti-biofouling performance of pressure retarded osmosis (PRO) by dosing with chlorhexidine gluconate, Desalination 481 (2020) 114376. https://doi.org/10.1016/j.desal.2020.114376.

[31] T.-S. Kim, P.-F. Sun, Y.G. Park, H.-D. Park, Effects of membrane and operational features on biofouling in a pressure retarded osmosis process, Desalination Water Treat. 97 (2017) 79-86

[32] K.-H. Park, P.-F. Sun, E.H. Kang, G.D. Han, B.J. Kim, Y. Jang, S.-H. Lee, J.H. Shim, H.-D. Park, Photocatalytic anti-biofouling performance of nanoporous ceramic membranes treated by atomic layer deposited ZnO, Sep. Purif. Technol. 272 (2021) 118935. https://doi.org/10.1016/j.seppur.2021.118935.

[33] E. Bar-Zeev, F. Perreault, A.P. Straub, M. Elimelech, Impaired performance of pressure-retarded osmosis due to irreversible biofouling, Environ. Sci. Technol. 49(21) (2015) 13050-8. https://doi.org/10.1021/acs.est.5b03523.

[34] X. Li, T. Cai, T.-S. Chung, Anti-fouling behavior of hyperbranched polyglycerol-grafted poly(ether sulfone) hollow fiber membranes for osmotic power generation, Environ. Sci. Technol. 48(16) (2014) 9898-9907. https://doi.org/10.1021/es5017262.

[35] T. Cai, X. Li, C.F. Wan, T.S. Chung, Zwitterionic polymers grafted poly(ether sulfone) hollow fiber membranes and their antifouling behaviors for osmotic power generation, J. Membr. Sci. 497 (2016) 142-152. https://doi.org/10.1016/j.memsci.2015.09.037.

[36] L. Qi, Y. Hu, Z. Liu, X. An, E. Bar-Zeev, Improved Anti-Biofouling Performance of Thin -Film Composite Forward-Osmosis Membranes Containing Passive and Active Moieties, Environ. Sci. Technol. 52(17) (2018) 9684-9693. https://doi.org/10.1021/acs.est.7b06382.

[37] L. Deng, Q. Wang, X. An, Z. Li, Y. Hu, Towards enhanced antifouling and flux performances of thin-film composite forward osmosis membrane via constructing a sandwich-like carbon nanotubes-coated support, Desalination 479 (2020) 114311. https://doi.org/10.1016/j.desal.2020.114311.

[38] M. Alhabeb, K. Maleski, B. Anasori, P. Lelyukh, L. Clark, S. Sin, Y. Gogotsi, Guidelines for Synthesis and Processing of Two-Dimensional Titanium Carbide (Ti3C2Tx MXene), Chem. Mater. 29(18) (2017) 7633-7644. https://doi.org/10.1021/acs.chemmater.7b02847.

[39] Y. Zhu, W. Xie, S. Gao, F. Zhang, W. Zhang, Z. Liu, J. Jin, Single-Walled Carbon Nanotube Film Supported Nanofiltration Membrane with a Nearly 10 nm Thick Polyamide Selective Layer for High-Flux and High-Rejection Desalination, Small 12(36) (2016) 5034-5041. https://doi.org/10.1002/smll.201601253.

[40] S.-Y. Ham, H.-S. Kim, Y. Jang, P.-F. Sun, J.-H. Park, J.S. Lee, Y. Byun, H.-D. Park, Control of membrane biofouling by 6-gingerol analogs: Quorum sensing inhibition, Fuel 250 (2019) 79-87. https://doi.org/10.1016/j.fuel.2019.03.145.

[41] J.H. Lee, E.-T. Yun, S.-Y. Ham, H.-S. Kim, P.-F. Sun, H.-D. Park, Electrically conductive carbon nanotube/graphene composite membrane for self-cleaning of biofouling via bubble generation, Desalination 535 (2022) 115841. https://doi.org/10.1016/j.desal.2022.115841.

[42] T.S. Kim, H.D. Park, Tributyl tetradecyl phosphonium chloride for biofouling control in reverse osmosis processes, Desalination 372 (2015) 39-46. https://doi.org/10.1016/j.desal.2015.06.019.

[43] D.M. Goeres, M.A. Hamilton, N.A. Beck, K. Buckingham-Meyer, J.D. Hilyard, L.R. Loetterle, L.A. Lorenz, D.K. Walker, P.S. Stewart, A method for growing a biofilm under low shear at the air–liquid interface using the drip flow biofilm reactor, Nat. Protoc. 4(5) (2009) 783-788. https://doi.org/10.1038/nprot.2009.59.

[44] Z. Wang, H.-C. Yang, F. He, S. Peng, Y. Li, L. Shao, S.B. Darling, Mussel-Inspired Surface Engineering for Water-Remediation Materials, Matter 1(1) (2019) 115-155. https://doi.org/10.1016/j.matt.2019.05.002.

[45] H. Lee, M. Dellatore Shara, M. Miller William, B. Messersmith Phillip, Mussel-Inspired Surface Chemistry for Multifunctional Coatings, Science 318(5849) (2007) 426-430. https://doi.org/10.1126/science.1147241.

[46] A. Miao, M. Wei, F. Xu, Y. Wang, Influence of membrane hydrophilicity on water permeability: An experimental study bridging simulations, J. Membr. Sci. 604 (2020) 118087. https://doi.org/10.1016/j.memsci.2020.118087.

[47] W. Yuan, A.L. Zydney, Humic Acid Fouling during Ultrafiltration, Environ. Sci. Technol. 34(23) (2000) 5043-5050. https://doi.org/10.1021/es0012366.

[48] Z. Yang, P.-F. Sun, X. Li, B. Gan, L. Wang, X. Song, H.-D. Park, C.Y. Tang, A Critical Review on Thin-Film Nanocomposite Membranes with Interlayered Structure: Mechanisms, Recent Developments, and Environmental Applications, Environ. Sci. Technol. 54(24) (2020) 15563-15583. https://doi.org/10.1021/acs.est.0c05377.

[49] X. Song, B. Gan, S. Qi, H. Guo, C.Y. Tang, Y. Zhou, C. Gao, Intrinsic Nanoscale Structure of Thin Film Composite Polyamide Membranes: Connectivity, Defects, and Structure–Property Correlation, Environ. Sci. Technol. 54(6) (2020) 3559-3569. https://doi.org/10.1021/acs.est.9b05892.

[50] S. Gao, Y. Zhu, Y. Gong, Z. Wang, W. Fang, J. Jin, Ultrathin Polyamide Nanofiltration Membrane Fabricated on Brush-Painted Single-Walled Carbon Nanotube Network Support for Ion Sieving, ACS Nano 13(5) (2019) 5278-5290. https://doi.org/10.1021/acsnano.8b09761.

[51] C.Y. Tang, Q. She, W.C.L. Lay, R. Wang, R. Field, A.G. Fane, Modeling double-skinned FO membranes, Desalination 283 (2011) 178-186. https://doi.org/10.1016/j.desal.2011.02.026.

[52] S. Qi, C.Q. Qiu, Y. Zhao, C.Y. Tang, Double-skinned forward osmosis membranes based on layer-by-layer assembly—FO performance and fouling behavior, J. Membr. Sci. 405-406 (2012) 20-29. https://doi.org/10.1016/j.memsci.2012.02.032.

[53] F. Perreault, H. Jaramillo, M. Xie, M. Ude, L.D. Nghiem, M. Elimelech, Biofouling Mitigation in Forward Osmosis Using Graphene Oxide Functionalized Thin-Film Composite Membranes, Environ. Sci. Technol. 50(11) (2016) 5840-8. https://doi.org/10.1021/acs.est.5b06364.

[54] X. Lu, X. Feng, J.R. Werber, C. Chu, I. Zucker, J.-H. Kim, C.O. Osuji, M. Elimelech, Enhanced antibacterial activity through the controlled alignment of graphene oxide nanosheets, Proc. Natl. Acad. Sci. U. S. A. 114(46) (2017) E9793. https://doi.org/10.1073/pnas.1710996114.

[55] A.F. Faria, C. Liu, M. Xie, F. Perreault, L.D. Nghiem, J. Ma, M. Elimelech, Thin-film composite forward osmosis membranes functionalized with graphene oxide–silver nanocomposites for biofouling control, J. Membr. Sci. 525 (2017) 146-156. https://doi.org/10.1016/j.memsci.2016.10.040.

[56] N.A. Weerasekara, K.H. Choo, C.H. Lee, Hybridization of physical cleaning and quorum quenching to minimize membrane biofouling and energy consumption in a membrane bioreactor, Water Res. 67 (2014) 1-10. https://doi.org/10.1016/j.watres.2014.08.049.

[57] D. Xu, X. Zhu, X. Luo, Y. Guo, Y. Liu, L. Yang, X. Tang, G. Li, H. Liang, MXene Nanosheet Templated Nanofiltration Membranes toward Ultrahigh Water Transport, Environ. Sci. Technol. (2020). https://doi.org/10.1021/acs.est.0c06835.

[58] J. Gutman, S.L. Walker, V. Freger, M. Herzberg, Bacterial Attachment and Viscoelasticity: Physicochemical and Motility Effects Analyzed Using Quartz Crystal Microbalance with Dissipation (QCM-D), Environ. Sci. Technol. 47(1) (2013) 398-404. https://doi.org/10.1021/es303394w.

[59] X. Zhang, Y. Guo, T. Wang, Z. Wu, Z. Wang, Antibiofouling performance and mechanisms of a modified polyvinylidene fluoride membrane in an MBR for wastewater treatment: Role of silver@silica nanopollens, Water Res. 176 (2020) 115749. https://doi.org/10.1016/j.watres.2020.115749.

[60] X. An, K. Zhang, Z. Wang, Q.V. Ly, Y. Hu, C. Liu, Improving the water permeability and antifouling property of the nanofiltration membrane grafted with hyperbranched polyglycerol, J. Membr. Sci. 612 (2020) 118417. https://doi.org/10.1016/j.memsci.2020.118417.

[61] C. Liu, Q. He, D. Song, J. Jackson, A.F. Faria, X. Jiang, X. Li, J. Ma, Z. Sun, Electroless deposition of copper nanoparticles integrates polydopamine coating on reverse osmosis membranes for efficient biofouling mitigation, Water Res. 217 (2022) 118375. https://doi.org/10.1016/j.watres.2022.118375.

[62] Z. Huang, Q. Zeng, Y. Liu, Y. Xu, R. Li, H. Hong, L. Shen, H. Lin, Facile synthesis of 2D TiO2@MXene composite membrane with enhanced separation and antifouling performance, J. Membr. Sci. 640 (2021) 119854. https://doi.org/10.1016/j.memsci.2021.119854.

[63] S. Shao, Y. Li, T. Jin, W. Liu, D. Shi, J. Wang, Y. Wang, Y. Jiang, J. Li, H. Li, Biofouling layer maintains low hydraulic resistances and high ammonia removal in the UF process operated at low flux, J. Membr. Sci. 596 (2020) 117612. https://doi.org/10.1016/j.memsci.2019.117612.

[64] R. Chen, H. Zhang, J. Wang, D. Xu, X. Tang, W. Gong, H. Liang, Insight into the role of biogenic manganese oxides-assisted gravity-driven membrane filtration systems toward emerging contaminants removal, Water Res. 224 (2022) 119111. https://doi.org/10.1016/j.watres.2022.119111.